Rheologica Acta (2024) 63:33–47
https://doi.org/10.1007/s00397-023-01422-y

ORIGINAL CONTRIBUTION

A novel approach for the fractional SLS material model experimental identification

Stefano Amadori[1] · **Giuseppe Catania**[2]

Received: 3 August 2023 / Revised: 10 November 2023 / Accepted: 10 November 2023 / Published online: 1 December 2023

Abstract

A multi-step, iterative technique for the local non-parametric identification of the standard linear solid (SLS) material model employing fractional order time differential operators is presented. Test input data consists of a set of identified material complex modulus values estimated at different frequency values, obtained from input–output experimental measurements made on a material specimen by means of forced harmonic excitation and from experimental measurements made on the same specimen in quasi-static relaxation conditions. The proposed technique is mainly based on an algebraic procedure leading to the solution of an overdetermined system of linear equations, in order to get the optimal value of the model unknown parameters. The procedure is non-parametric, since the SLS model order is initially unknown. The optimal model size can be found by evaluating the stability properties of the solution associated to any model size and by automatically discarding computational, non-physical contributions. The identification procedure is first validated by means of numerically simulated test data from within known model examples, and then it is applied to some experimentally obtained test data associated to different materials.

Keywords Fractional material model · Non-parametric identification · Relaxation test · Forced vibrational test

Introduction

The multi-axial $\boldsymbol{\sigma}$ stress versus $\boldsymbol{\varepsilon}$ strain tensor material model requires some assumptions to be made with respect to the material behavior, e.g., local plane or stress deformation, isotropic or anisotropic material, among all (Timoshenko et al. 1974; Tschoegl 1989). If an isotropic material is taken into account, at least two parameters are needed to identify the material multiaxial $\boldsymbol{\sigma}=\boldsymbol{\sigma}(\boldsymbol{\varepsilon})$ model. These two independent parameters can be chosen among the $E(\omega)$ Young's modulus, the $\nu(\omega)$ Poisson coefficient, and the $G(\omega)$ shear modulus, ω being to the angular frequency. Uniaxial stress and shear dynamical tests can be made to obtain the numerical estimates of these material parameters by using standard experimental measuring systems (Waterman 1977; Tschoegl 1989; Hilton 2017; Leon and Chen 2019).

This paper is focused on a technique for the $E(\omega)$ model identification from within uniaxial stress measurements. If the Poisson coefficient is assumed to be stationary with respect to frequency and known in advance, as it occurs in many engineering applications, then the full material $\boldsymbol{\sigma}=\boldsymbol{\sigma}(\boldsymbol{\varepsilon})$ model identification only results from the $E(\omega)$ model identification. It can be outlined that the technique proposed herein may be adopted, in principle, to identify $G(\omega)$ from within uniaxial shear measurements as well. Experimentally estimated $E(\omega)$ values can be obtained by means of input–output dynamic and quasi-static measurements (Findley et al. 1989; Swaminathan and Shivakumar 2009; Placet and Foltete 2010) on structural material specimens, in different uniaxial experimental set-ups (Menard 2008; Amadori and Catania 2017). Input–output frequency response functions (FRFs) can be obtained by harmonically exciting a specimen in forced vibration conditions at a known excitation frequency. The applied force, the response amplitude, and its time delay with respect to the excitation are

✉ Stefano Amadori
stefano.amadori4@unibo.it

Giuseppe Catania
giuseppe.catania@unibo.it

[1] Ciri-Mam, University of Bologna, Viale Risorgimento 2, 40136 Bologna, BO, Italy

[2] DIN, Department of Industrial Engineering, Ciri-Mam, University of Bologna, Viale Risorgimento 2, 40136 Bologna, BO, Italy

measured in correspondence of known axial positions. From the measured FRF data, $E(\omega)$ can then be estimated by taking into account of the beam specimen mechanical model (Timoshenko et al. 1974, Read and Dean 1978, McAninch et al. 2015, Schalnat et al. 2020). The dynamic contribution of the beam distributed inertia, of the mobile measuring subsystem lumped inertia, and of the instrument frame-fixture system should also be taken into account, and a calibration procedure, proposed by these authors in a previous work (Amadori and Catania 2022), can be used to accomplish this task.

Commercially available FRF dynamic measuring systems typically work in a limited $\Omega = [f_{\min} = 0.1, f_{\max} = 300]$ Hz frequency range. Nevertheless, a wide experimental frequency range is generally needed to improve the accuracy and the application range of the material model to be identified, but $E(\omega)$ estimates at $f < f_{\min}$ cannot be practically obtained from dynamical measurements because of experimental time limitations. Quasi-static measurements can be used and processed in order to estimate $E(\omega)$ in the low $[0, f_{\min}]$ frequency range. Known algorithms (Kwon et al. 2016) can be employed to convert compliance data, obtained from quasi-static creep measurements in the time domain, into $E(\omega)$ values in the frequency domain.

When dealing with anisotropic materials, it should be outlined that more than two material parameters are generally required to model the linear multi-axial $\boldsymbol{\sigma}$ stress versus $\boldsymbol{\varepsilon}$ strain tensor material, e.g., twenty-one material parameters in the general anisotropic case, reducing to nine in the orthotropic case and to five material parameters in the transversely isotropic case. It can also be found that some relationships between these parameters, expressed by means of inequalities, may also apply because of thermodynamic constraints (Bagley and Torvik 1986). The experimental estimate of these anisotropic material parameters from within dynamical I/O measurements may be a complex task, since the material properties such as the principal orthotropy directions may vary pointwise in the bulk material. Non-standard measuring apparatus involving non-standard experimental specimen geometries, a large number of experimental dofs as well as optical full-field measuring sensors and digital processing techniques were proposed for this task (Chen et al. 2016; Schemmann et al. 2018; Fu et al. 2020). Once the value of the material parameters is experimentally found in a wide frequency range, the identification procedure proposed in this work can be generalized and applied to model these materials estimated parameters as well.

In this work, the $E(\omega)$ complex modulus is modeled by means of the fractional SLS material model assumption. According to Ferry (1961), the SLS model does not provide any insight into the underlying microscopic material physics. It should be outlined that such a material mechanical model only describes its macroscopic behavior and that different equivalent mechanical models can be adopted as well for the same purposes. Molecular and microscopic-based material models can be considered as well (Ferry 1961; Hill 1972) for some materials such as metal polycrystals, but their application to the dynamical simulation of the behavior of structures made of the material under study typically requires strong assumptions and high computational efforts, making such engineering applications practically unfeasible.

The identification of a fractional SLS material model is a more challenging task than the identification of a standard SLS model. Some approaches, mainly based on the use of nonlinear optimization fitting techniques, were proposed in the past (Pritz 2003; Papoulia et al. 2010; Katicha and Flintsch 2012; Katsourinis and Kontou 2019): the model order is assumed to be a priori known, and the resulting optimal model parameter solution strongly depends on the initially assumed value of the optimization unknown parameters. Some researchers formulated strategies for evaluating the initial choice of the unknown parameters by tentatively extrapolating it from experimental measurements, but such strategies did not show to be general enough to be adopted in any context and typically require that low-order fractional SLS material models only should be considered (Pritz 2004; Katicha and Flintsch 2012; Katsourinis and Kontou 2019).

It can be found that the $E(\omega)$ fractional SLS material model can be expressed as the ratio of two pseudo-polynomial functions where non-integer powers of the $(j \cdot \omega)$ variable, $j = \sqrt{-1}$, are dealt with. A parametric algebraic technique based on Levy's approach was proposed in the past (Kapp et al. 2020) to identify the coefficients of the rational pseudo-polynomials, whose maximum order is assumed to be known in advance. Nevertheless, the optimal model order and the value of the parameters associated to each fractional SLS element do not result from the application of this approach.

In this work, a novel procedure able to effectively identify the optimal fractional material model from within $E(\omega)$ experimental estimates in a wide frequency range, covering a quasi-static behavior, is proposed. A fractional SLS material model is taken into account, but no a priori assumption is made on the derivative fractional order associated to each fractional SLS element and on the number of fractional SLS elements, so that a local non-parametric identification procedure results. A procedure able to estimate the $E(\omega)$ contribution in the low frequency range from within creep relaxation measurements is also described.

Non-parametric identification of the fractional SLS material model

Fractional SLS material model assumptions

The fractional SLS material model taken into account in this work is depicted in Fig. 1. It is composed of N

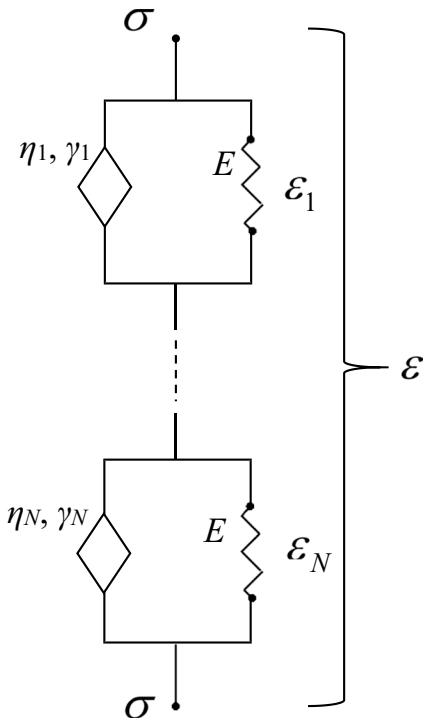

Fig. 1 Fractional SLS model

fractional Kelvin elements arranged in series, where N is also assumed to be the model order. The i-th fractional Kelvin element is defined by the E_i elastic parameter, the η_i fractional viscous parameter, and the γ_i non-integer, fractional differentiation order. In the time domain, the $\varepsilon_i(t)$ strain response associated to the i-th SLS element satisfies the following differential equation:

$$\sigma(t) = E_i \cdot \left(\varepsilon_i(t) + \frac{\eta_i}{E_i} \cdot \frac{\partial^{\gamma_i}\left(\varepsilon_i(t)\right)}{\partial t^{\gamma_i}} \right) \tag{1}$$

and when a σ_0 stress step is applied, i.e., $\sigma(t<0)=0$ and $\sigma(t\geq 0)=\sigma_0$, $\varepsilon_i(t)$ is (Koeller 1984; Katicha and Flintsch 2012)

$$\varepsilon_i(t) = \frac{\sigma_0}{E_i} \cdot \left(1 - M_{\gamma_i}\left(\left(-\frac{t}{\tau_i} \right)^{\gamma_i} \right) \right) \; ; \; \tau_i = \left(\frac{\eta_i}{E_i} \right)^{\frac{1}{\gamma_i}}. \tag{2}$$

$M_{\gamma_i}()$ refers to the classic Mittag–Leffler function, coinciding with the exponential function if $\gamma_i \equiv 1$ (Gorenflo et al. 2014):

$$M_{\gamma_i}(z) = \sum_{k=0}^{\infty} \frac{z^k}{\Gamma\left(k \cdot \gamma_i + 1\right)}, \tag{3}$$

where $\Gamma()$ is the gamma function. The total $J(t)=\varepsilon(t)/\sigma_0$ creep compliance can be estimated as follows:

$$J(t) = \frac{\varepsilon(t)}{\sigma_0} = \frac{1}{\sigma_0} \cdot \sum_{i=1}^{N} \varepsilon_i(t) = \sum_{i=1}^{N} \frac{1}{E_i} \cdot \left(1 - M_{\gamma i}\left(\left(-\frac{t}{\tau_i} \right)^{\gamma i} \right) \right). \tag{4}$$

In the frequency domain, by applying the $\widehat{()}$ Fourier transform operator to Eq. 1,

$$\widehat{\sigma} = \left[E_i + \eta_i \cdot (j \cdot \omega)^{\gamma_i} \right] \widehat{\varepsilon}_i, i = 1, \ldots, N. \tag{5}$$

From Eq. 5, the $\hat{\varepsilon}(\omega)/\hat{\sigma}(\omega)$ material strain–stress relationship is

$$\frac{\hat{\varepsilon}}{\hat{\sigma}}(\omega) = E^{-1}(\omega) = \sum_{i=1}^{N} \frac{1}{E_i + \eta_i \cdot (j \cdot \omega)^{\gamma_i}}. \tag{6}$$

Some assumptions are made: the E_i elastic and η_i viscous parameters are real positive-valued parameters, and the γ_i exponent is also real-valued, $\gamma_i \in]0, 1]$. A standard Kelvin element results if $\gamma_i = 1$, and a Hooke element results if $\gamma_i = 0$.

It is assumed that γ_i is approximated by a fractional value:

$$\gamma_i = \frac{n_i}{\Lambda}, \; 1 \leq n_i \leq \Lambda, \tag{7}$$

$n_i, \Lambda \in \mathbb{N}$ and Λ is assumed to be high enough to fit any γ_i unknown exponent value, $i = 1,\ldots,N$. From Eqs. 6 and 7,

$$\begin{aligned} E^{-1}(\omega) &= \sum_{i=1}^{N} \frac{1/\eta_i}{(j\cdot\omega)^{\frac{n_i}{\Lambda}} + \frac{E_i}{\eta_i}} = \sum_{i=1}^{N} \frac{\Upsilon_i}{p^{n_i} + \lambda_i}, \\ \lambda_i &= \frac{E_i}{\eta_i} \in \mathfrak{R}^+, \; p = (j \cdot \omega)^{\frac{1}{\Lambda}}, \; \Upsilon_i = \frac{1}{\eta_i} \in \mathfrak{R}^+. \end{aligned} \tag{8}$$

Since

$$\begin{aligned} p^{n_i} + \lambda_i &= \prod_{r=1}^{n_i} (p - z_r^i), \qquad z_r^i = \left(\lambda_i\right)^{\frac{1}{n_i}} \cdot e^{\frac{j\cdot\pi}{n_i}\cdot(2\cdot r-1)}, \; \left|z_r^i\right| = \left(\lambda_i\right)^{\frac{1}{n_i}}; \; r = 1, ..., n_i; i = 1, ..., N \\ &\arg\left(z_{r+1}^i\right) - \arg\left(z_r^i\right) = \frac{2\cdot\pi}{n_i}, \; r = 1, ..., n_i - 1; \end{aligned} \tag{9}$$

the i-th term from the Eq. 8 sum can also be expressed in partial fraction form as follows:

$$\frac{\Upsilon_i}{p^{n_i}+\lambda_i}=\frac{\Upsilon_i}{\prod_{r=1}^{n_i}(p-z_r^i)}=\sum_{r=1}^{n_i}\frac{\upsilon_r^i}{p-z_r^i}, \tag{10}$$

so that the following $E^{-1}(\omega)=\hat{\varepsilon}(\omega)/\hat{\sigma}(\omega)$ equivalent strain–stress relationship of a N order fractional SLS model results

$$E^{-1}(\omega)=\sum_{i=1}^{N}\sum_{r=1}^{n_i}\frac{\upsilon_r^i}{(j\cdot\omega)^{\frac{1}{\Lambda}}-z_r^i}=\sum_{i=1}^{N}\sum_{r=1}^{n_i}\frac{\upsilon_r^i}{p-z_r^i}=\Theta(p). \tag{11}$$

A $\boldsymbol{\Upsilon}$ set of fractional SLS material parameters, $\mathbf{Y}=\{\upsilon_r^i,\ z_r^i,\ n_i,\ i=1,...,N,\ r=1,...,n_i\}$ results from Eq. 11, being fully equivalent to the $\boldsymbol{\Xi}$ set, $\boldsymbol{\Xi}=\{n_i,\ E_i,\ \eta_i,\ i=1,\ldots,N\}$ from Eq. 6. From Eq. 11, $\Theta(p)$ can be expressed in partial fraction form and as the ratio of two polynomials, in the p complex variable, or as the ratio of two pseudo-polynomials with fractional order exponents, in the imaginary $(j\cdot\omega)$ variable:

$$\Theta(p)=\sum_{i=1}^{N}\left(\sum_{r=1}^{n_i}\frac{\upsilon_r^i}{p-z_r^i}\right)=\sum_{i=1}^{m}\frac{\upsilon_i}{p-z_i}=\frac{\sum_{i=0}^{m-1}p^i\cdot\alpha_i}{p^m+\sum_{i=0}^{m-1}p^i\cdot\beta_i}=\frac{p^{m-1}\cdot\alpha_{m-1}+...+\alpha_0}{p^m+p^{m-1}\cdot\beta_{m-1}+...+\beta_0}=$$
$$=\frac{\sum_{i=0}^{m-1}(j\cdot\omega)^{\frac{i}{\Lambda}}\cdot\alpha_i}{(j\cdot\omega)^{\frac{m}{\Lambda}}+\sum_{i=0}^{m-1}(j\cdot\omega)^{\frac{i}{\Lambda}}\cdot\beta_i}=\frac{(j\cdot\omega)^{\frac{m-1}{\Lambda}}\cdot\alpha_{m-1}+...+\alpha_0}{(j\cdot\omega)^{\frac{m}{\Lambda}}+(j\cdot\omega)^{\frac{m-1}{\Lambda}}\cdot\beta_{m-1}+...+\beta_0}=E^{-1}(j\cdot\omega), \tag{12}$$

where from Eqs. 8, 10, and 12, since $E_i,\ \eta_i\in\Re^+$:

$$\boldsymbol{\alpha}=\left[\alpha_o,...,\alpha_{m-1}\right]^T\in\Re^+,\quad \boldsymbol{\beta}=\left[\beta_o,...,\beta_{m-1}\right]^T\in\Re^+,\quad m=\sum_{i=1}^{N}n_i. \tag{13}$$

The $\mathbf{z}$ pole and $\boldsymbol{\upsilon}$ residue fractional SLS model sets are

$$\boldsymbol{\upsilon}=\left[\upsilon_1,...,\upsilon_i,...,\upsilon_m\right]=\left[\upsilon_1^1,...,\upsilon_{n_1}^1,...,\upsilon_1^N,...\upsilon_{n_N}^N\right],$$
$$\mathbf{z}=\left[z_1,...,z_i,...,z_m\right]=\left[z_1^1,...,z_{n_1}^1,...,z_1^N,...,z_{n_N}^N\right], \tag{14}$$
$$\overline{\mathbf{Y}}=\{\boldsymbol{\upsilon},\mathbf{z}\}.$$

Identification of the $\overline{\mathbf{Y}}$ parameter set of the fractional SLS material model

An algebraic technique able to identify the $\overline{\mathbf{Y}}$ fractional SLS model parameters from $E^{-1}(\omega_k)=\Theta(p_k)=\Theta_k$, $k=1,\ldots,N_{em}$ measurement estimates, $\omega_k\in\boldsymbol{\omega}=[\omega_1,...,\omega_{N_{em}}]$, is now introduced. The algebraic approach proposed by Levy (1959) is here adopted.

From Eq. 12,

$$\Theta_k=\frac{\sum_{i=0}^{m-1}\left(p_k\right)^i\cdot\alpha_i}{\left(p_k\right)^m+\sum_{i=0}^{m-1}\left(p_k\right)^i\cdot\beta_i},\qquad k=1,...,N_{em}. \tag{15}$$

A system of N_{em} linear equations in $(\boldsymbol{\alpha},\boldsymbol{\beta})$, $2\cdot m$ real unknowns, results

$$\sum_{i=0}^{m-1}\left(p_k\right)^i\cdot\alpha_i-\sum_{i=0}^{m-1}\Theta_k\cdot\left(p_k\right)^i\cdot\beta_i=\Theta_k\cdot\left(p_k\right)^m, \tag{16}$$

where m is assumed to be unknown at the identification stage.

From Eq. 16, a Vandermonde-like linear system in the $\boldsymbol{\alpha},\boldsymbol{\beta}$ unknowns results, so that an ill-conditioned numerical problem may result if m is high or if $\max(\boldsymbol{\omega})/\min(\boldsymbol{\omega})$ is high as well. The computational accuracy of the Eq. 16 system solution can be improved by introducing a normalized u real variable:

$$u_k=\frac{|p_k|}{\left|p_{N_{em}}\right|},\quad u_k\in[0,1], \tag{17}$$

$$p_k=|p_k|\cdot e^{j\cdot\varphi}=u_k\cdot\left|p_{N_{em}}\right|\cdot e^{j\cdot\varphi},\ \left(p_k\right)^i$$
$$=\left(u_k\right)^i\cdot\left|p_{N_{em}}\right|^i\cdot e^{j\cdot\varphi\cdot i},\quad\varphi=\frac{\pi}{2\cdot\Lambda}. \tag{18}$$

Combining Eqs. 12–15,

$$\begin{aligned}&\sum_{i=0}^{m-1}\left(u_k\right)^i\cdot\left|p_{N_{em}}\right|^i e^{j\cdot\varphi\cdot i}\alpha_i-\sum_{i=0}^{m-1}\Theta_k\cdot\left(u_k\right)^i\cdot\left|p_{N_{em}}\right|^i\cdot e^{j\cdot\varphi\cdot i}\cdot\beta_i=\Theta_k\cdot\left(u_k\right)^m\cdot\left|p_{N_{em}}\right|^m\cdot e^{j\cdot\varphi\cdot m}\\&\sum_{i=0}^{m-1}\left(u_k\right)^i\cdot e^{j\cdot\varphi\cdot(i-m)}\cdot\chi_i-\sum_{i=0}^{m-1}\Theta_k\cdot\left(u_k\right)^i\cdot e^{j\cdot\varphi\cdot(i-m)}\mu_i=\Theta_k\cdot\left(u_k\right)^m\qquad,\quad k=1,\ldots,N_{em}\\&\chi_i=\left|p_{N_{em}}\right|^{i-m}\cdot\alpha_i,\quad\mu_i=\left|p_{N_{em}}\right|^{i-m}\cdot\beta_i\ .\end{aligned}\tag{19}$$

Since from Eq. 16 $\chi_i,\ \mu_i\in\Re,\ \forall i$, in compact form, a linear system of N_{em} complex equations in real unknowns results

$$\begin{aligned}&\left[\begin{array}{cc}\mathbf{A}&-\mathbf{B}\end{array}\right]\cdot\left[\begin{array}{c}\boldsymbol{\chi}\\\boldsymbol{\mu}\end{array}\right]=\mathbf{C};\\&\boldsymbol{\chi}=\left[\begin{array}{cccc}\chi_0&\ldots&\chi_i&\ldots\ \chi_{m-1}\end{array}\right]^T,\ \boldsymbol{\mu}=\left[\begin{array}{cccc}\mu_0&\ldots&\mu_i&\ldots\ \mu_{m-1}\end{array}\right]^T,\\&\mathbf{A}=\left[\begin{array}{cccc}e^{-j\cdot\varphi\cdot m}&u_1\cdot e^{j\cdot\varphi\cdot(1-m)}&\ldots&\left(u_1\right)^{m-1}\cdot e^{-j\cdot\varphi}\\\ldots&\ldots&\ldots&\ldots\\e^{-j\cdot\varphi\cdot m}&u_{N_{em}}\cdot e^{j\cdot\varphi\cdot(1-m)}&\ldots&\left(u_{N_{em}}\right)^{m-1}\cdot e^{-j\cdot\varphi}\end{array}\right],\\&\mathbf{B}=\left[\begin{array}{cccc}\Theta_1\cdot e^{-j\cdot\varphi\cdot m}&\Theta_1\cdot u_1\cdot e^{j\cdot\varphi\cdot(1-m)}&\ldots&\Theta_1\cdot\left(u_1\right)^{m-1}\cdot e^{-j\cdot\varphi}\\\ldots&\ldots&\ldots&\ldots\\\Theta_{N_{em}}\cdot e^{-j\cdot\varphi\cdot m}&\Theta_{N_{em}}\cdot u_{N_{em}}\cdot e^{j\cdot\varphi\cdot(1-m)}&\ldots&\Theta_{N_{em}}\cdot\left(u_{N_{em}}\right)^{m-1}\cdot e^{-j\cdot\varphi}\end{array}\right],\\&\mathbf{C}=\left[\begin{array}{cccc}\Theta_1\cdot\left(u_1\right)^m&\ldots&\Theta_{N_{em}}\cdot\left(u_{N_{em}}\right)^m\end{array}\right]^T.\end{aligned}\tag{20}$$

From Eq. 20, a linear system of $2{\cdot}N_{em}$ real equations in $2{\cdot}m$ real unknowns results as well:

$$\left[\begin{array}{cc}\mathrm{Re}(\mathbf{A})&-\mathrm{Re}(\mathbf{B})\\\mathrm{Im}(\mathbf{A})&-\mathrm{Im}(\mathbf{B})\end{array}\right]\cdot\left[\begin{array}{c}\boldsymbol{\chi}\\\boldsymbol{\mu}\end{array}\right]=\left[\begin{array}{c}\mathrm{Re}(\mathbf{C})\\\mathrm{Im}(\mathbf{C})\end{array}\right].\tag{21}$$

The $\{\boldsymbol{\chi},\ \boldsymbol{\mu}\}$ unknown parameters can be obtained by least squares solving of Eq. 21 by means of a singular value decomposition (SVD) based technique, and $\{\boldsymbol{\alpha},\ \boldsymbol{\beta}\}$ unknowns result as well:

$$\alpha_i=\left|p_{N_{em}}\right|^{m-i}\cdot\chi_i,\quad\beta_i=\left|p_{N_{em}}\right|^{m-i}\cdot\mu_i.\tag{22}$$

The $\{\boldsymbol{\alpha},\boldsymbol{\beta}\}=\{\boldsymbol{\alpha},\boldsymbol{\beta}\}_m$ solution can be found in principle with respect to any m assumed value. The $\overline{\mathbf{Y}}_m=\{\mathbf{z},\ \boldsymbol{\upsilon}\}$ associated poles and residues can be found as well by means of the following steps. The z_i poles are the m zeros of the following polynomial function:

$$z^m+z^{m-1}\cdot\beta_{m-1}+\ldots+\beta_0=0\tag{23}$$

and the υ_i, $i=1,\ldots,m$ system residues can be evaluated as follows:

$$\upsilon_i=\lim_{p\to z_i}\left[\sum_{r=1}^{m}\frac{\upsilon_r}{p-z_r}\cdot\left(p-z_i\right)\right]=\frac{\sum_{r=0}^{m-1}\alpha_r\cdot\left(z_i\right)^r}{\prod_{\substack{r=1\\r\neq i}}^{m}\left(z_i-z_r\right)}.\tag{24}$$

Identification of the Ξ parameter set of the fractional SLS material model

From Eqs. 9 and 10,

$$\begin{aligned}&\upsilon_r^i=\lim_{p\to z_r^i}\left[\frac{\Upsilon_i\cdot\left(p-z_r^i\right)}{\prod_{s=1}^{n_i}\left(p-z_s^i\right)}\right]=\frac{\Upsilon_i}{\prod_{\substack{s=1\\s\neq r}}^{n_i}\left(z_r^i-z_s^i\right)},\\&\prod_{\substack{s=1\\s\neq r}}^{n_i}\left(z_r^i-z_s^i\right)=\frac{\Upsilon_i}{\upsilon_r^i}.\end{aligned}\tag{25}$$

$$\begin{aligned}&p^{n_i}+\lambda_i=\prod_{s=1}^{n_i}\left(p-z_s^i\right)\\&\frac{p^{n_i}+\lambda_i}{p-z_r^i}=\prod_{\substack{s=1\\s\neq r}}^{n_i}\left(p-z_s^i\right),\quad p\neq z_r^i,\end{aligned}\tag{26}$$

and from Eqs. 10 and 26,

$$\lim_{p\to z_r^i}\left(\frac{p^{n_i}+\lambda_i}{p-z_r^i}\right)=\prod_{\substack{s=1\\s\neq r}}^{n_i}\left(z_r^i-z_s^i\right)=\frac{\Upsilon_i}{\upsilon_r^i}.\tag{27}$$

A new $\Psi(p)$ function can be defined as follows:

$$\psi(p)=p^{n_i},\ \psi\left(z_r^i\right)=\left(z_r^i\right)^{n_i}=-\lambda_i;\ r=1,\ldots,n_i.\tag{28}$$

It follows that

$$\frac{d\psi}{dp}\left(z_r^i\right) = n_i \cdot \left(z_r^i\right)^{n_i-1} = n_i \frac{\left(z_r^i\right)^{n_i}}{z_r^i} = -\frac{n_i \cdot \lambda_i}{z_r^i}, \tag{29}$$

and from Eqs. 27–29,

$$\frac{d\psi}{dp}\left(z_r^i\right) = \lim_{p\to z_r^i} \frac{\psi(p) - \psi\left(z_r^i\right)}{p - z_r^i} = \lim_{p\to z_r^i} \left(\frac{p^{n_i} + \lambda_i}{p - z_r^i}\right) = \frac{\Upsilon_i}{v_r^i}. \tag{30}$$

The following result can be obtained:

$$v_r^i = -\frac{\Upsilon_i \cdot z_r^i}{n_i \cdot \lambda_i}, \tag{31}$$

and from Eqs. 8 and 31,

$$v_r^i = -\frac{z_r^i}{n_i \cdot E_i},\ r = 1...n_i,\ i = 1...N. \tag{32}$$

It results that the modulus and argument of any v_i pole satisfy the following conditions from Eqs. 9 and 32:

$$\left|v_r^i\right| = \frac{1}{n_i \cdot E_i} \cdot \left(\frac{E_i}{\eta_i}\right)^{\frac{1}{n_i}} = \frac{1}{n_i \cdot \left(\lambda_i \cdot E_i^{n_i-1}\right)^{\frac{1}{n_i}}},$$
$$\arg\left(v_{r+1}^i\right) - \arg\left(v_r^i\right) = \frac{2\cdot\pi}{n_i},\quad \arg\left(v_r^i\right) = \arg\left(z_r^i\right) + \pi. \tag{33}$$

The E_i, η_i material model element parameters are thus found to satisfy the following conditions as well (Eqs. 8–9, 31–33):

$$E_i = -\frac{z_r^i}{v_r^i \cdot n_i} = \frac{\left|z_r^i\right|}{\left|v_r^i\right| \cdot n_i},\qquad \eta_i = \frac{E_i}{\left|z_r^i\right|^{n_i}} = \frac{\left|z_r^i\right|^{1-n_i}}{\left|v_r^i\right| n_i},\ \forall r. \tag{34}$$

Equation 34 defines the relationship between the $\boldsymbol{\Upsilon}_m$ and $\boldsymbol{\Xi}_m$ parameter sets.

The $\{\overline{\mathbf{z}}^i, \overline{\boldsymbol{\upsilon}}^i\} \in \{\mathbf{z}, \boldsymbol{\upsilon}\}_m$ pole and residue subset, associated to the i-th fractional SLS material model element with $n_i > 1$, $n_i = size(\overline{\mathbf{z}}^i) = size(\overline{\boldsymbol{\upsilon}}^i)$, $\overline{\mathbf{z}}^i = [\overline{z}_1^i, ..., \overline{z}_{n_i}^i]$, $\overline{\boldsymbol{\upsilon}}^i = [\overline{v}_1^i, ..., \overline{v}_{n_i}^i]$, must satisfy, by means of tolerances associated to the expected experimental and numerical noise, the following conditions obtained from Eqs. 9 and 33:

$$\left|\overline{z}_1^i\right| \approx \left|\overline{z}_r^i\right|,\quad \arg\left(\overline{z}_r^i\right) - \arg\left(\overline{z}_{r-1}^i\right) \approx \frac{2\cdot\pi}{n_i},$$
$$\left|\overline{v}_1^i\right| \approx \left|\overline{v}_r^i\right|,\quad \arg\left(\overline{v}_r^i\right) - \arg\left(\overline{v}_{r-1}^i\right) \approx \frac{2\cdot\pi}{n_i},\ r = 2, ..., n_i, \tag{35}$$
$$\arg\left(\overline{z}_1^i\right) \approx \frac{\pi}{n_i},\quad \arg\left(\overline{v}_1^i\right) \approx \arg\left(\overline{z}_1^i\right) + \pi.$$

The (E_i, η_i, γ_i) material parameters, from the i-th single fractional SLS element, can be obtained from the $\left\{\overline{\mathbf{z}}_i, \overline{\boldsymbol{\upsilon}}_i\right\}$ identified sets by using the results found in Eqs. 8 and 34:

$$E_i = \frac{\sum_{r=1}^{n_i}\left|\overline{z}_r^i\right|}{\sum_{r=1}^{n_i}\left|\overline{v}_r^i\right| n_i},\qquad \eta_i = E_i \cdot \left(\frac{n_i}{\sum_{r=1}^{n_i}\left|\overline{z}_r^i\right|}\right)^{n_i},\qquad \gamma_i = \frac{n_i}{\Lambda}. \tag{36}$$

Defining $\{\overline{\mathbf{z}}, \overline{\boldsymbol{\upsilon}}\}_m = \{\{\overline{\mathbf{z}}^1, \overline{\boldsymbol{\upsilon}}^1\}, ..., \{\overline{\mathbf{z}}^i, \overline{\boldsymbol{\upsilon}}^i\}, ...\}$, the $\{\underline{\mathbf{z}}, \underline{\boldsymbol{\upsilon}}\}_m$ pole and residue elements from $\{\mathbf{z}, \boldsymbol{\upsilon}\}_m$ that does not belong to $\{\overline{\mathbf{z}}, \overline{\boldsymbol{\upsilon}}\}_m$ result from $\{\mathbf{z}, \boldsymbol{\upsilon}\}_m = \{\{\overline{\mathbf{z}}, \overline{\boldsymbol{\upsilon}}\}_m, \{\underline{\mathbf{z}}, \underline{\boldsymbol{\upsilon}}\}_m\}$.

The $\{\underline{\mathbf{z}}^i, \underline{\boldsymbol{\upsilon}}^i\} \in \{\underline{\mathbf{z}}, \underline{\boldsymbol{\upsilon}}\}_m$ poles and residues associated to the $n_i = 1$ fractional SLS material model elements must satisfy, by means of the same previously indicated tolerance values, the following conditions:

$$\arg\left(\underline{z}_1^i\right) \approx \pi,\quad \arg\left(\underline{v}_1^i\right) \approx 0. \tag{37}$$

The E_i, η_i, γ_i model element parameters can be found from Eq. 36, $\eta_i = 1$:

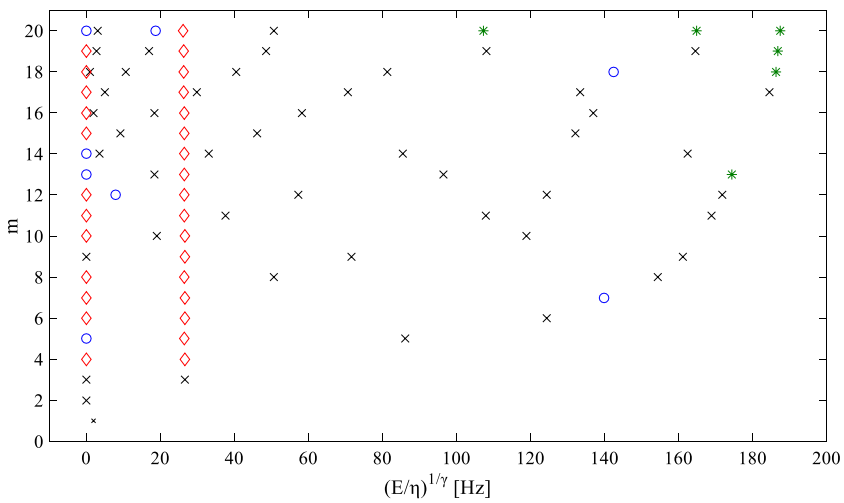

Fig. 2 Stability plot example

Table 1 Ξ_m solution stability conditions

Stability condition	Graphical marker
Stable solution	◊
(γ, E) locally stable solution	*
(γ, η) locally stable solution	○
Unstable solution	×

$$E_i = \left|\frac{\underline{z}_1^i}{\underline{v}_1^i}\right|, \quad \eta_i = \frac{E_i}{\left|\underline{z}_1^i\right|}, \quad \gamma_i = \frac{1}{\Lambda}. \tag{38}$$

A Ξ_m set of model parameters, corresponding to N_m fractional SLS elements, is found: $\Xi_m = \{(E_1, \eta_1, \gamma_1), ..., (E_{N_m}, \eta_{N_m}, \gamma_{N_m})\}$. It must be outlined that since the solutions obtained from Eqs. 36 and 38 satisfy the Eqs. 35 and 37 conditions, most of the computational solutions, i.e., the ones not associated to a physical material behavior, are virtually eliminated by following this approach. Nevertheless, different N_m order, material physical solution sets can be obtained with respect to any arbitrarily assumed m value, and the optimal N material model order is still not known at this stage.

Identification of the optimal material model order

The N optimal order value can be found by performing the identification approach, discussed in previous sections, for $m = 1,\ldots,m_{\max}$.

The solution stability of the $\{E_i, \eta_i, \gamma_i\}_m \in \Xi_m$ parameter set related to i-th element is evaluated with respect to any element of Ξ_{m-1}. The $\{E_i, \eta_i, \gamma_i\}_m \in \Xi_m$ solution is stable with respect to $\{E_s, \eta_s, \gamma_s\}_{m-1} \in \Xi_{m-1}$ if $(\gamma_i)_m = (\gamma_s)_{m-1}$ and $(E_i, \eta_i,)_m$ approximately coincides with $(E_s, \eta_s,)_{m-1}$ by means of a user-defined tolerance. This stability evaluation can be automatically performed. A stability plot graphical procedure can also be used to show the effectiveness of this procedure, and an example of a stability plot is shown in Fig. 2. The $(E_i, \eta_i, \gamma_i)_m$ solutions are plotted with respect to the $(E/\eta)^{1/\gamma} = (E_i/\eta_i)^{1/\gamma_i}$ abscissa and to the m ordinate value, by means of a graphical symbol associated to its stability properties. The meaning of the different symbols employed is detailed in Table 1, i.e., a stable solution must satisfy the previously defined conditions with respect to (γ, E, η), e.g., a (γ_i, E_i) locally stable solution must satisfy the stability conditions with respect to (γ, E), a (γ_i, η_i) locally stable solution must satisfy the stability conditions with respect to (γ, η), and a plotted unstable solution satisfies the stability conditions with respect to γ only. The total number of stable (E_i, η_i, γ_i), $i = 1,\ldots,N$, selected element solutions coincide with the optimal N material model order.

$E^{-1}(j\cdot\omega)$ experimental estimates from forced vibration and creep relaxation measurements

In this work, material $E^{-1}(\omega)$ experimental estimates are obtained from both forced vibration test and creep relaxation test data. Uniform slender beam specimens, homogeneously made of the material under study, were tested by means of a TA Instruments DMAQ800 system (Fig. 3) in flexural, clamped sliding equivalent boundary conditions and in isothermal conditions. In the forced vibration tests, beam applied force and displacement output were both measured at the mobile beam specimen end, and the maximum applied strain is taken constant by means of a

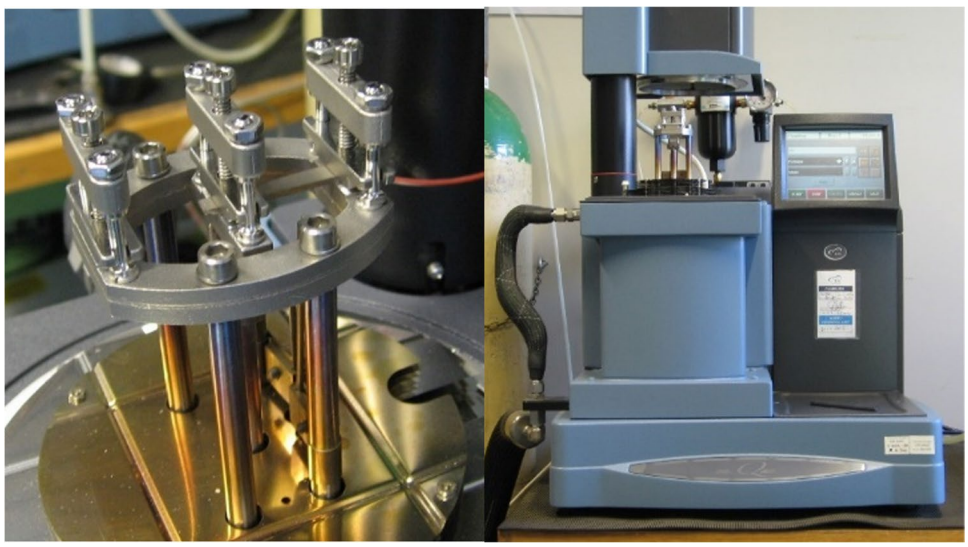

Fig. 3 Experimental measurement test system

closed loop control strategy. The value of the maximum applied strain is taken low enough to satisfy the assumption of linear material behavior with respect to any material under test.

$E^{-1}(\omega)$ complex modulus estimates are obtained in the $\Omega_H = [0.1, 200]$ Hz discrete frequency set from input–output FRF data by means of the previously cited calibration procedure presented by these authors, taking into account the dynamic contribution of the beam distributed inertia, of the mobile measuring subsystem lumped inertia and of the instrument frame system.

Creep measurements are made by applying a step excitation at the mobile beam specimen end, L being the beam length. Both excitation and response are measured in the $[0, t_{max}]$ discrete time set, N_C discrete values, where t_{max} is chosen at the measurement stage depending on the expected material creep behavior. $\sigma_{max}(t_i, x = L) = \sigma_0$ flexural maximum axial stress and $\varepsilon_{max}(t_i, x = L)$ flexural maximum axial strain measurements are estimated at the mobile beam end by means of the previously cited calibration procedure, and $J_i = J(t_i) = \varepsilon_{max}(t_i, L)/\sigma_0$, $i = 0, \ldots, N_C\text{-}1$, compliance test data are estimated as well.

$E^{-1}(\omega_k)$, $k = 1, \ldots, N_L$, complex modulus estimates in the low frequency range can be estimated from $J(t)$ creep compliance discrete data by means of the following procedure, mainly based on the algorithm developed by Evans et al. (2009) and here adapted to the case of solid viscoelastic materials.

By Fourier transforming the $J(t)$ response to a unitary step:

$$\widehat{J}(\omega) = \frac{1}{j \cdot \omega \cdot E(\omega)} \tag{39}$$

but $\widehat{J}(\omega)$ cannot be numerically estimated from discrete $J(t)$ measured values since $J(t)$ is not absolutely integrable over the time interval $[-\infty, \infty]$. By applying the Fourier transform operator to $J''(t) = d^2J(t)/dt^2$ instead, the convergence of the Fourier operator can be easily obtained:

$$\widehat{J}''(\omega) = \frac{j \cdot \omega}{E(\omega)} \tag{40}$$

From Eq. 40, by substituting the numerical estimate of $J''(t_i)$ from J_i, $i = 0, \ldots, N_C\text{-}1$ creep time relaxation compliance discrete test data, the following formula can be adopted to obtain $E^{-1}(\omega_k)$ complex modulus estimates for any ω_k angular frequency:

$$E^{-1}(\omega_k) = \frac{1}{j \cdot \omega_k} \cdot \left(\sum_{i=1}^{N_C-1} \left(\frac{J_i - J_{i-1}}{t_i - t_{i-1}} \right) \cdot \left(e^{-j \cdot \omega_k \cdot t_{i-1}} - e^{-j \cdot \omega_k \cdot t_i} \right) \right); \; J_0 = 0, \; t_0 = 0. \tag{41}$$

It must be outlined that both the $[0, \ldots, t_i, \ldots, t_{N_{C-1}}]$ time set and the $[\omega_1, \ldots, \omega_k, \ldots, \omega_{N_L}]$ frequency set do not need to be uniformly spaced.

Application examples

Identification from numerically simulated measurements

Two NC1 and NC2 simulated measurement test cases, obtained from within analytical known model data whose reference parameters are reported in Table 2, are used to validate the identification procedure.

A set of $N_H = 200$ measurements are numerically simulated in the medium to high $\Omega_H = [0.1, 200]$ Hz frequency

Table 2 Numerical test cases

NC1 test case	Model parameters	Reference model	$(IM)_H$ identified model	$(IM)_F$ identified model
	N	2	1	2
	γ_i	0.33 0.66	0.66	0.33 0.66
	E_i [Pa]	$7.3 \cdot 10^8$ $1.1 \cdot 10^9$	$8.935 \cdot 10^8$	$5.95 \cdot 10^8$ $8.89 \cdot 10^8$
	η_i [Pa•s$^{\gamma i}$]	$1.69 \cdot 10^{10}$ $3.78 \cdot 10^7$	$2.944 \cdot 10^7$	$1.43 \cdot 10^{10}$ $2.96 \cdot 10^7$
	$E_0 / E(\omega)$ mean quadratic error		$6.3 \cdot 10^{-2}$	$4.9 \cdot 10^{-5}$
NC2 test case	γ_i	0.25 0.5	0.25	0.25 0.5
	E_i [Pa]	$5.9 \cdot 10^{10}$ $7.4 \cdot 10^{10}$	$5.55 \cdot 10^{10}$	$5.56 \cdot 10^{10}$ $6.39 \cdot 10^{10}$
	η_i [Pa•s$^{\gamma i}$]	$1.35 \cdot 10^{10}$ $2.08 \cdot 10^{12}$	$1.28 \cdot 10^{10}$	$1.29 \cdot 10^{10}$ $1.96 \cdot 10^{12}$
	$E_0 / E(\omega)$ mean quadratic error		$6.1 \cdot 10^{-2}$	$7.6 \cdot 10^{-4}$

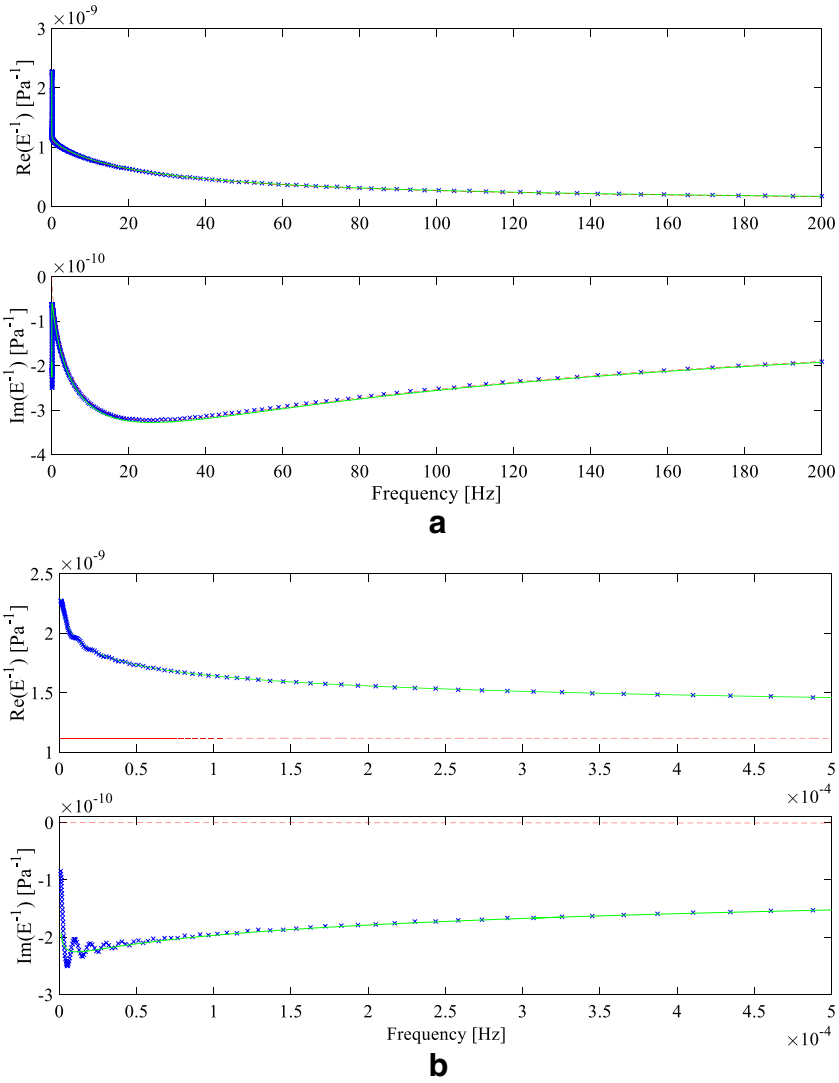

Fig. 4 **a** NC1 test case: $E^{-1}(\omega_k)$ numerical estimate (blue), $E^{-1}(\omega)$ model fit estimate from the $(IM)_H$ (red) and the $(IM)_F$ (green) identified models. **b** NC1 test case: $E^{-1}(\omega_k)$ numerical estimate (blue), $E^{-1}(\omega)$ model fit estimate from the $(IM)_H$ (red) and the $(IM)_F$ (green) identified models, $f_k \in [0, 5{\cdot}10^{-4}]$ Hz

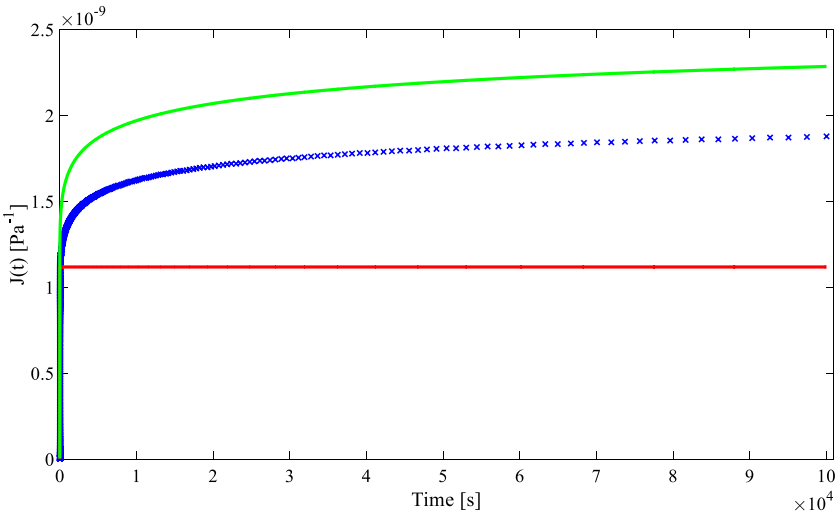

Fig. 5 NC1 test case: J_i numerical estimates (blue), $J(t)$ model fit estimate from the $(IM)_H$ (red) and the $(IM)_F$ (green) identified models

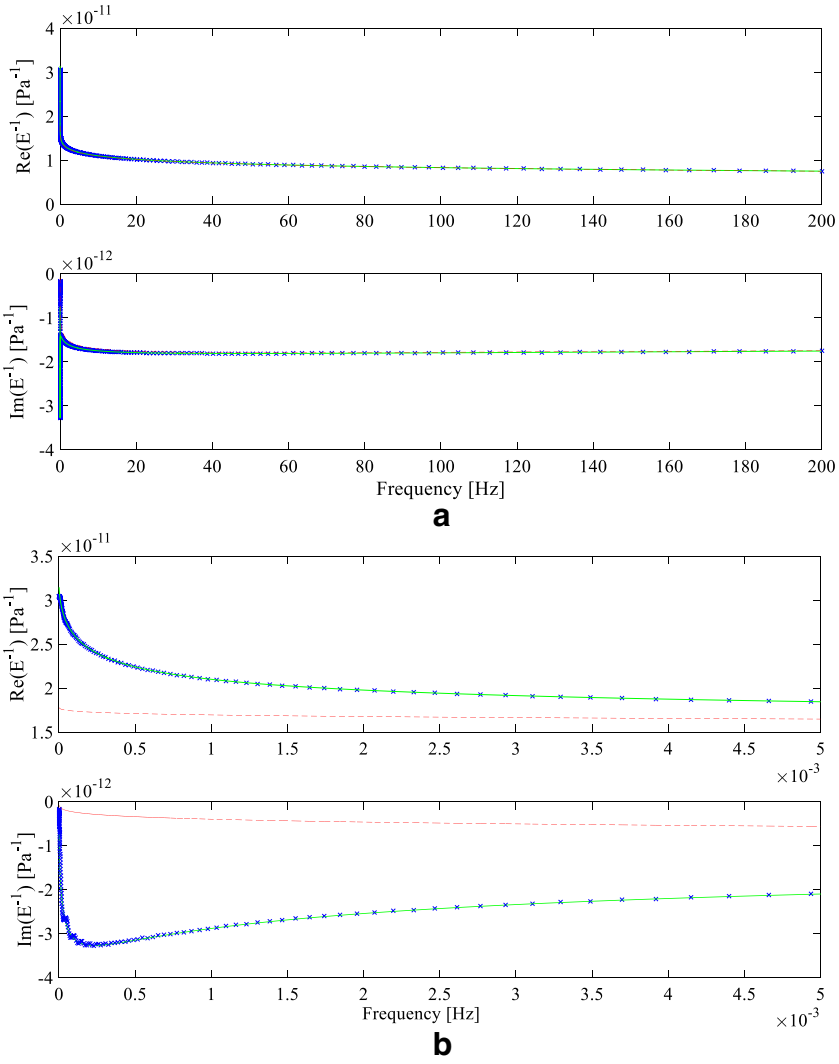

Fig. 6 **a** NC2 test case: $E^{-1}(\omega_k)$ numerical estimate (blue), $E^{-1}(\omega)$ model fit estimate from the $(IM)_H$ (red) and the $(IM)_F$ (green) identified models. **b** NC2 test case: $E^{-1}(\omega_k)$ numerical estimate (blue), $E^{-1}(\omega)$ model fit estimate from the $(IM)_H$ (red) and the $(IM)_F$ (green) identified models, $f_k \in [0, 5{\cdot}10^{-3}]$ Hz

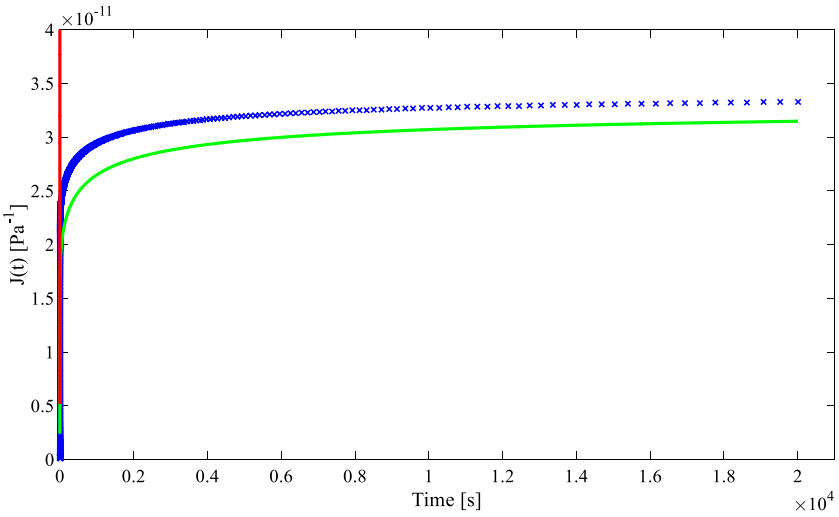

Fig. 7 NC2 test case: J_i numerical estimates (blue), $J(t)$ model fit estimate from the $(IM)_H$ (red) and the $(IM)_F$ (green) identified models

range by means of Eq. 3. $E(\omega_k)$ estimates, $N_L = 200$, in the $\Omega_L = [10^{-6}, 0.1]$ Hz frequency range, are obtained by applying Eq. 41 to $N_C = 1000$, $t_{max} = 10^5$ s, numerically simulated J_i compliance measurements (Eq. 4). Random numerical noise was added to the simulated measurements, S/N = 120 dB average signal-to-noise ratio.

Table 2 reports the identification results obtained with respect to the NC1 and NC2 test cases. $(IM)_H$ refers to the identification results obtained with respect to the test data in the partial Ω_H frequency range, while $(IM)_F$ refers to the identification results obtained with respect to the test data in the full $\Omega_F = \{\Omega_L, \Omega_H\}$ frequency range.

Table 3 Beam specimens data

Material	Length [m]	Section area [m^2]	Density [kg/m^3]
EC1	$1.785 \cdot 10^{-2}$	$1.7 \cdot 10^{-5}$	$1.02 \cdot 10^3$
EC2	$1.785 \cdot 10^{-2}$	$9.3 \cdot 10^{-6}$	$1.15 \cdot 10^3$

The following parameters of the previously described identification procedure were chosen for the NC1 test case: $\Lambda = 6$, $m_{max} = 18$ for both the $(IM)_H$ and $(IM)_F$ identification steps. The following parameters of the previously described identification procedure were chosen for the NC2 test case: $\Lambda = 4$, $m_{max} = 15$ for both the $(IM)_H$ and $(IM)_F$ identification steps.

Figures 4a and b show the $E^{-1}(\omega_k)$ virtual measurement test data versus the analytically estimated values from the identified $(IM)_H$ and $(IM)_F$ models, NC1 test case. Figure 5 shows the $J(t_i)$ creep compliance virtual measurement test data versus the analytically estimated values from the identified $(IM)_H$ and $(IM)_F$ models, NC1 test case.

Figures 6a and b show the $E^{-1}(\omega_k)$ virtual measurement test data versus the analytically estimated values from the identified $(IM)_H$ and $(IM)_F$ models, NC2 test case. Figure 7 shows the $J(t_i)$ creep compliance virtual measurement test data versus the analytically estimated values from the identified $(IM)_H$ and $(IM)_F$ models, NC2 test case.

Table 4 Experimental test cases

EC1 material	$(IM)_H$ identified model	$(IM)_F$ identified model
N	4	5
γ_i	0.5 0.5 1 1	0.5 0.5 1 1 1
E_i [Pa]	$5.426 \cdot 10^6$ $9.262 \cdot 10^7$ $9.013 \cdot 10^9$ $8.588 \cdot 10^9$	$5.025 \cdot 10^6$ $1.037 \cdot 10^6$ $6.266 \cdot 10^9$ $1.189 \cdot 10^{10}$ $2.465 \cdot 10^{10}$
η_i [Pa•$s^{\gamma i}$]	$1.784 \cdot 10^7$ $4.092 \cdot 10^6$ $2.131 \cdot 10^7$ $7.396 \cdot 10^6$	$1.667 \cdot 10^7$ $3.404 \cdot 10^6$ $1.435 \cdot 10^7$ $1.395 \cdot 10^7$ $2.094 \cdot 10^7$
$E_0 / E(\omega)$ mean quadratic error	$2.695 \cdot 10^{-2}$	$3.557 \cdot 10^{-4}$
EC2 material	$(IM)_H$ identified model	$(IM)_F$ identified model
N	1	5
γ_i	0.25	0.25 0.5 0.5 0.5 1
E_i [Pa]	$1.181 \cdot 10^9$	$1.518 \cdot 10^9$ $7.163 \cdot 10^{10}$ $2.316 \cdot 10^9$ $4.707 \cdot 10^{11}$ $1.591 \cdot 10^{12}$
η_i [Pa•$s^{\gamma i}$]	$5.813 \cdot 10^8$	$5.657 \cdot 10^8$ $3.127 \cdot 10^{11}$ $6.888 \cdot 10^9$ $3.529 \cdot 10^{10}$ $2.505 \cdot 10^9$
$E_0 / E(\omega)$ mean quadratic error	$5.79e \cdot 10^{-3}$	$8.7 \cdot 10^{-2}$

An excellent agreement of the identified models with respect to the virtual measurement data was obtained for both test cases in the frequency and in the time domain when the full Ω frequency range is taken into account.

Identification from experimental measurements

Two experimental test cases, referring to the EC1 and EC2 materials, are considered. The EC1 material was obtained by mixing a commercially available epoxy dual component resin, Loxeal 31–10®, and recycled carbon fibers (length 60 to 300 μm) with the following volume ratios: 30% for 31 component, 60% for 10 component, and 10% for recycled carbon fibers. The EC2 material was obtained by mixing a commercially available epoxy dual component resin material, Milliput®, with the 66–33% volume ratios between the hardener and the resin component.

The tested specimens data are reported in Table 3. The test temperature was held uniform, $T = 35$ °C, during all experimental test steps.

With respect to the EC1 material, $J(t)$ creep compliance measurements were done according to the following test parameters: $N_C = 48$ logarithmically spaced time values, $t_{max} = 2.9 \cdot 10^3$ s, $\sigma_0 = 5 \cdot 10^4$ Pa. With respect to EC2 material, $J(t)$ creep measurements were done according to the following test parameters: $N_C = 45$ logarithmically spaced time values, $t_{max} = 1.68 \cdot 10^3$ s, $\sigma_0 = 5 \cdot 10^4$ Pa. For both the EC1 and EC2 materials under test, $E^{-1}(\omega)$ estimates in the low $\Omega_L = [10^{-6}, 0.1]$ Hz frequency range, $N_L = 110$ not uniformly spaced frequency values were obtained by means of Eq. 41 from the J_i estimates.

For both the EC1 and the EC2 test materials, $E^{-1}(\omega)$ estimates were obtained from forced flexural vibration measurements in the medium to high $\Omega_H = [0.1, 200]$ Hz frequency

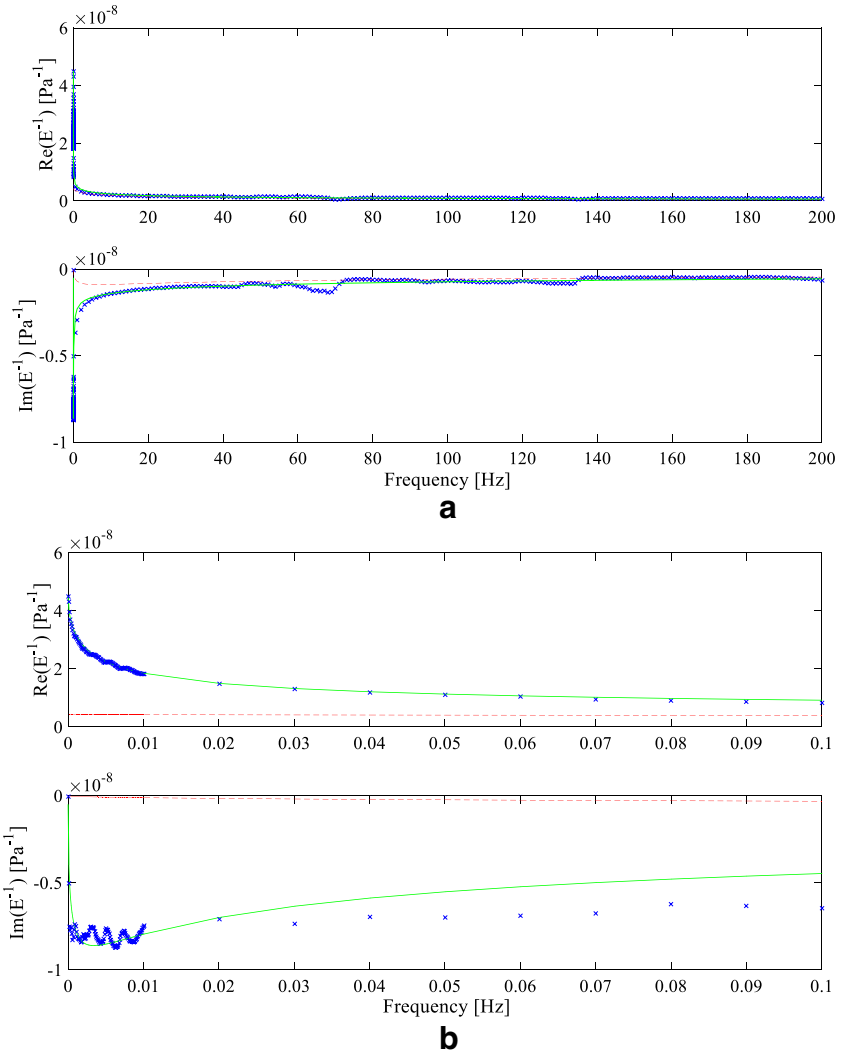

Fig. 8 **a** EC1 test case: $E^{-1}(\omega_k)$ experimental measurement (blue), $E^{-1}(\omega)$ model fit estimate from the $(IM)_H$ (red) and the $(IM)_F$ (green) identified models. **b** EC1 test case, $E^{-1}(\omega_k)$ experimental measurement (blue), $E^{-1}(\omega)$ model fit estimate from the $(IM)_H$ (red) and the $(IM)_F$ (green) identified models, $f_k \in [0,0.1]$ Hz

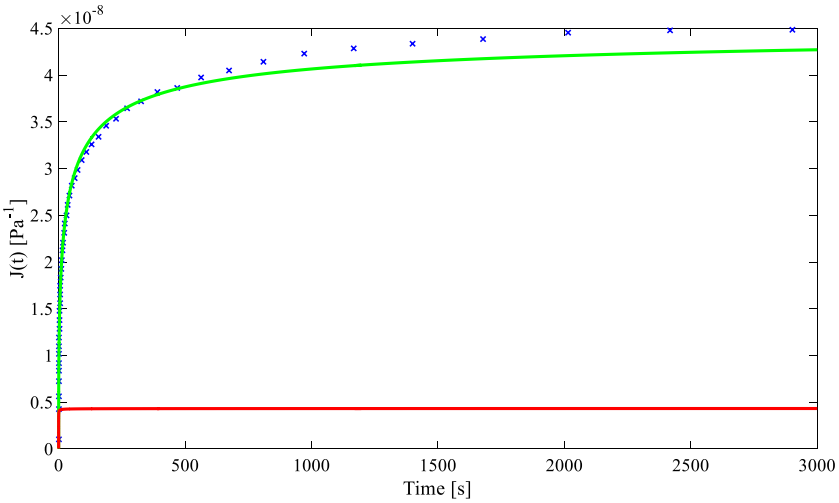

Fig. 9 EC1 test case: J_i experimental measurements (blue), $J(t)$ model fit estimate from the $(IM)_H$ (red) and the $(IM)_F$ (green) identified models

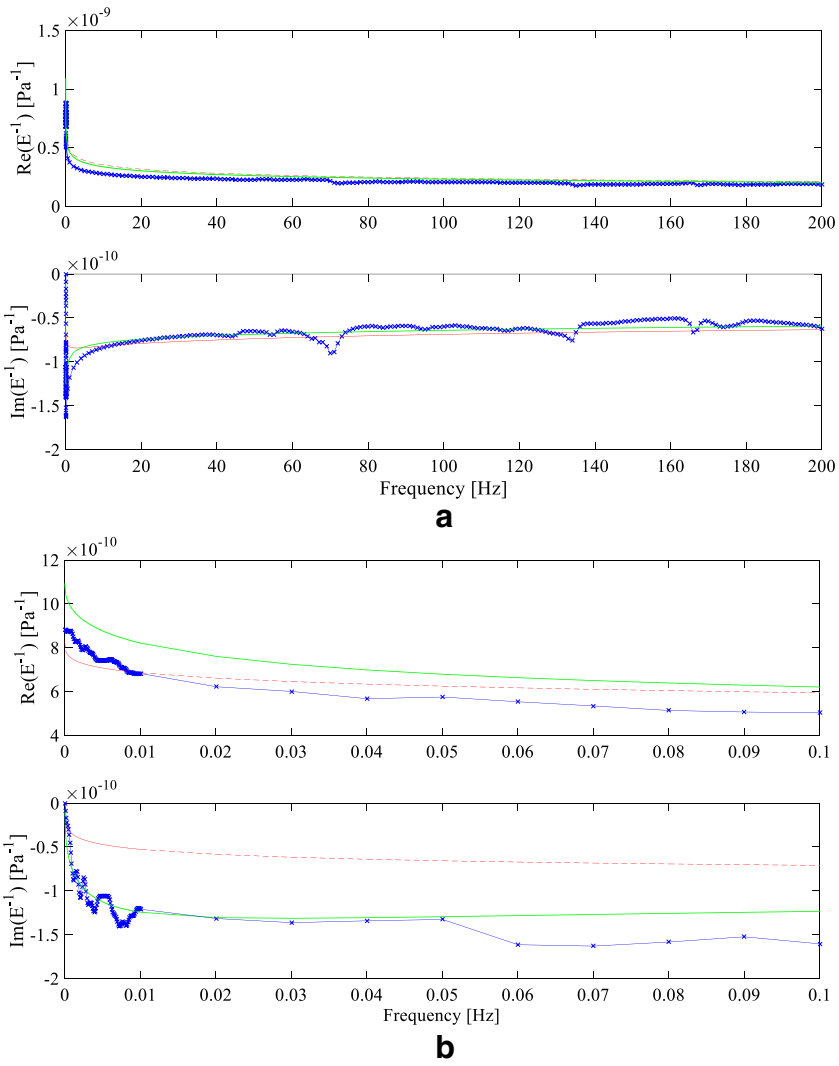

Fig. 10 **a** EC2 test case: $E^{-1}(\omega_k)$ experimental measurement (blue), $E^{-1}(\omega)$ model fit estimate from the $(IM)_H$ (red) and the $(IM)_F$ (green) identified models. **b** EC2 test case: $E^{-1}(\omega_k)$ experimental measurement (blue), $E^{-1}(j\omega)$ model fit estimate from the $(IM)_H$ (red) and the $(IM)_F$ (green) identified models, $f_k \in [0,0.1]$ Hz

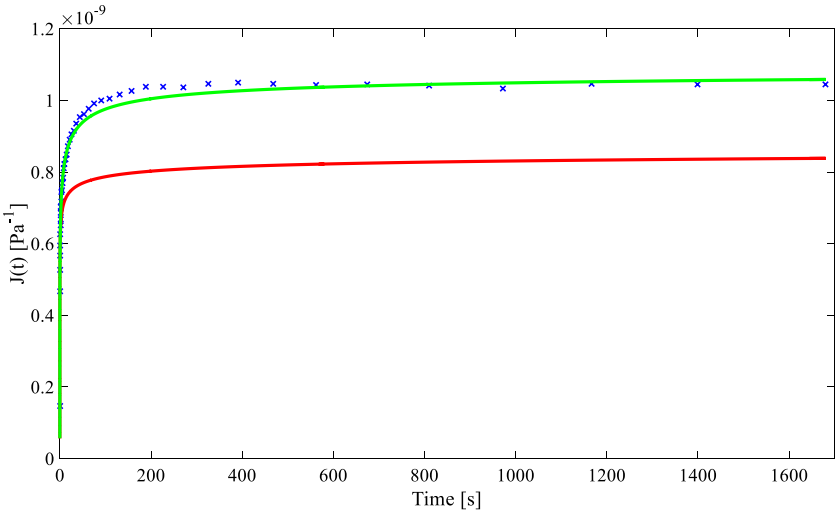

Fig. 11 EC2 test case: J_i experimental measurements (blue), $J(t)$ model fit estimate from the $(IM)_H$ (red) and the $(IM)_F$ (green) identified models

range, $N_H = 202$ not uniformly spaced frequency values, 0.05% maximum strain.

Table 4 reports the identification results obtained with respect to the EC1 and EC2 test cases. $(IM)_H$ refers to the identification results obtained with respect to test data in the partial Ω_H frequency range, while $(IM)_F$ refers to the identification results obtained with respect to the test data in the full $\Omega_F = \{\Omega_L, \Omega_H\}$ frequency range. The following parameters of the previously described identification procedure were chosen for the EC1 test case: $\Lambda = 4$, $m_{max} = 25$ for both the $(IM)_H$ and the $(IM)_F$ identification steps. The following parameters of the previously described identification procedure were chosen for the EC2 test case: $\Lambda = 4$ $m_{max} = 25$ for both the $(IM)_H$ and the $(IM)_F$ identification steps.

Figure 8a and b show the $E^{-1}(\omega_k)$ experimental measurement test data values versus the analytically estimated values from the identified $(IM)_H$ and $(IM)_F$ models, EC1 test case. Figure 9 shows the J_i creep compliance experimental measurement test data values versus the analytically estimated values from the identified $(IM)_H$ and $(IM)_F$ models, EC1 test case.

Figure 10a and b show the $E^{-1}(\omega_k)$ experimental measurement test data values versus the analytically estimated values from the identified $(IM)_H$ and $(IM)_F$ models, EC2 test case. Figure 11 shows the J_i creep compliance experimental measurement test data values versus the analytically estimated values from the identified $(IM)_H$ and $(IM)_F$ models, EC2 test case.

In both the experimental test cases proposed, the identified model fits are in good agreement with the experimental data, and it must be outlined that the $(IM)_F$ model identification results show a significant improvement in accuracy with respect to the $(IM)_H$ model identification results in both the frequency and the time domain.

Conclusions

A technique for the experimental identification of the $E(\omega)$ fractional SLS material model, made up of a series arrangement of Kelvin elements with fractional time derivative operators, is presented. The technique is non-parametric since the number of SLS elements is not assumed to be a priori known, but it can be obtained from the identification procedure.

The Levy algebraic approach is adopted to obtain a well-conditioned system of linear equations in the frequency domain that can be solved by a least square SVD-based procedure. A stability approach is adopted to obtain the optimal material model order.

Nonphysical solutions resulting from computational and experimental noise can be automatically discarded, so that a minimum order SLS fractional model is expected to result by applying the proposed technique.

The identification procedure was first validated by means of two numerical test cases in a wide frequency, not uniformly spaced, frequency range, and accurate identification results were obtained. Numerical noise was added to check the robustness of the identification procedure. The procedure was then applied by means of experimental data estimates in a wide frequency range, obtained from forced vibration measurements and from creep compliance measurements. Two experimental test cases related to some composite polymeric materials were considered, and the identified equivalent material models showed to effectively fit the experimental measurements in both the frequency and the time domain.

Acknowledgements Technical support from Andrea Zucchini, Danilo Persici from Marzocchi Pompe S.p.A., Casalecchio di Reno, Italy, and from Massimo Penatti and Alessandra Maino from Loxeal s.r.l. is kindly acknowledged.

Funding Open access funding provided by Alma Mater Studiorum - Università di Bologna within the CRUI-CARE Agreement.

Declarations

Competing interests The authors declare no competing interests.

References

Amadori S, Catania G (2017) Robust identification of the mechanical properties of viscoelastic non standard materials by means of frequency domain experimental measurements. Compos Struct 169:79–89. https://doi.org/10.1016/j.compstruct.2016.11.029

Amadori S, Catania G (2022) Experimental identification of the material standard linear solid model parameters by means of dynamical measurements. J Vib Control 28(23–24):3688–3704. https://doi.org/10.1177/10775463211037151

Bagley RL, Torvik PJ (1986) On the fractional calculus model of viscoelastic behavior. J Rheol 30:133–155. https://doi.org/10.1122/1.549887

Chen K, Scales M, Kyriakides S, Corona E (2016) Effects of anisotropy on material hardening and burst in the bulge test. Int J Solids Struct 82:70–84. https://doi.org/10.1016/j.ijsolstr.2015.12.012

Evans RML, Tassieri M, Auhl D, Waigh TA (2009) Direct conversion of rheological compliance measurements into storage and loss moduli. Phys Rev E 80:012501

Ferry JD (1961) Viscoelastic properties of polymers. John Wiley & Sons Inc., New York

Findley WN, Lai JS, Onaran K (1989) Creep and relaxation of nonlinear viscoelastic materials. Dover publications Inc., New York

Fu J, Xie W, Zhou J, Qi L (2020) A method for the simultaneous identification of anisotropic yield and hardening constitutive parameters for sheet metal forming. Int J Mech Sci 181:105756. https://doi.org/10.1016/j.ijmecsci.2020.105756

Gorenflo R, Kilbas AA, Mainardi F, Rogosin SV (2014) Mittag-Leffler functions, Related topics and applications. Springer, New York

Hill R (1972) On constitutive macro-variables for heterogeneous solids at finite strain. Proc Royal Soc London. Ser A, Math Phys Sci 326(1565):131–147 (http://www.jstor.org/stable/78044)

Hilton HH (2017) Elastic and viscoelastic Poisson's ratios: the theoretical mechanics perspective. Mater Sci Appl 8:291–332. https://doi.org/10.4236/msa.2017.84021

Kapp D, Weise F, Ruderman M, Reger J (2020) Fractional-order system identification of viscoelastic behavior: a frequency domain based experimental study. IEEE 16th International Workshop on Advanced Motion Control (AMC), Kristiansand, Norway, 153–160. https://doi.org/10.1109/AMC44022.2020.9244449

Katicha SW, Flintsch GW (2012) Fractional viscoelastic models: master curve construction, interconversion, and numerical approximation. Rheol Acta 51:675–689. https://doi.org/10.1007/s00397-012-0625-y

Katsourinis S, Kontou E (2019) Fractional viscoelastic for interconverting linear viscoelastic functions of various polymeric structures. Rheol Acta 58(2019):307–309. https://doi.org/10.1007/s00397-019-01146-y

Koeller RC (1984) Application of fractional calculus to the theory of viscoelasticity. J Appl Mech 51:299–307. https://doi.org/10.1115/1.3167616

Kwon MK, Lee SH, Lee SG, Cho KS (2016) Direct conversion of creep data to dynamic moduli. J Rheol 60:1181–1197

Leon G, Chen HL (2019) Direct determination of dynamic elastic modulus and Poisson's ratio of Timoshenko rods. Vibration 2(1):157–173. https://doi.org/10.3390/vibration2010010

Levy EC (1959) Complex-curve fitting. IRE Transact Automat Control AC-4(1):37–43. https://doi.org/10.1109/TAC.1959.6429401

McAninch IM, Palmese GR, Lenhart JL, La Scala JJ (2015) DMA testing of epoxy resins: the importance of dimensions. Polym Eng Sci 55:2761–2774

Menard KP (2008) Dynamic mechanical analysis: a practical introduction, 2nd edn. CRC Press, Boca Raton, Florida

Papoulia K, Panoskaltsis V, Kurup N, Korovajchuk I (2010) Rheological representation of fractional order viscoelastic material models. Rheol Acta 49:381–400. https://doi.org/10.1007/s00397-010-0436-y

Placet V, Foltete E (2010) Is Dynamic Mechanical Analysis (DMA) a non-resonance technique? The European physical journal conferences 6:41004. In: Proceedings of the 14th international conference on experimental mechanics (ICEM14), Boca Raton, Florida

Pritz T (2003) Five-parameter fractional derivative model for polymeric damping materials. J Sound Vib 265(5):935–952. https://doi.org/10.1016/S0022-460X(02)01530-4

Pritz T (2004) Frequency power law of material damping. Appl Acoust 65:1027–1036. https://doi.org/10.1016/j.apacoust.2004.06.001

Read BE, Dean GD (1978) The determination of dynamic properties of polymers and composites. Adam Hilger Ltd, Bristol, England

Schalnat J, Garoz Gómez D, Daelemans L, De Baere I, De Clerck K, Van Paepegem W (2020) Influencing parameters on measurement accuracy in dynamic mechanical analysis of thermoplastic polymers and their composites. Polymer Testing 91:106799. https://doi.org/10.1016/j.polymertesting.2020.106799

Schemmann M, Lang J, Helfrich A, Seelig T, Böhlke T (2018) Cruciform specimen design for biaxial tensile testing of SMC. J Compos Sci 2(1):12. https://doi.org/10.3390/jcs2010012

Swaminathan G, Shivakumar K (2009) A re-examination of DMA testing of polymer matrix composites. J Reinf Plast Compos 28(8):979–994. https://doi.org/10.1177/0731684407087740

Timoshenko S, Young DH, Weaver W (1974) Vibration problems in engineering. John Wiley & Sons Inc., New York

Tschoegl NW (1989) The phenomenological theory of linear viscoelastic behavior. Springer-Verlag, Berlin

Waterman HA (1977) Relations between loss angles in isotropic linear viscoelastic materials. Rheol Acta 16:31–42. https://doi.org/10.1007/BF01516927